

Nonlinear hyperspectral unmixing with robust nonnegative matrix factorization

Cédric Févotte and Nicolas Dobigeon

Abstract—This paper introduces a robust mixing model to describe hyperspectral data resulting from the mixture of several pure spectral signatures. This new model not only generalizes the commonly used linear mixing model, but also allows for possible nonlinear effects to be easily handled, relying on mild assumptions regarding these nonlinearities. The standard nonnegativity and sum-to-one constraints inherent to spectral unmixing are coupled with a group-sparse constraint imposed on the nonlinearity component. This results in a new form of robust nonnegative matrix factorization. The data fidelity term is expressed as a β -divergence, a continuous family of dissimilarity measures that takes the squared Euclidean distance and the generalized Kullback-Leibler divergence as special cases. The penalized objective is minimized with a block-coordinate descent that involves majorization-minimization updates. Simulation results obtained on synthetic and real data show that the proposed strategy competes with state-of-the-art linear and nonlinear unmixing methods.

Index Terms—Hyperspectral imagery, nonlinear unmixing, robust nonnegative matrix factorization, group-sparsity.

I. INTRODUCTION

Spectral unmixing (SU) is an issue of prime interest when analyzing hyperspectral data since it provides a comprehensive and meaningful description of the collected measurements in various application fields including remote sensing [1], planetology [2], food monitoring [3] or spectro-microscopy [4]. SU consists in decomposing P multi-band observations $\mathbf{Y} = [\mathbf{y}_1, \dots, \mathbf{y}_P]$ into a collection of K individual spectra $\mathbf{M} = [\mathbf{m}_1, \dots, \mathbf{m}_K]$, called *endmembers*, and estimating their relative proportions (or *abundances*) $\mathbf{A} = [\mathbf{a}_1, \dots, \mathbf{a}_P]$ in each observation [5], [6]. Most of the hyperspectral unmixing algorithms proposed in the signal & image processing and geoscience literatures rely on the commonly admitted linear mixing model (LMM), $\mathbf{Y} \approx \mathbf{M}\mathbf{A}$. Indeed, LMM provides a good approximation of the physical process underlying the observations and has resulted in interesting results for most applications. However, for several specific applications, LMM may be inaccurate and other nonlinear models need to be advocated [7]. For instance, in remotely sensed images composed of vegetation (e.g., trees), interactions of photons with multiple components of the scene lead to nonlinear effects that can be taken into account

using bilinear models [8], [9]. As explained in [10], several bilinear models have been proposed [11]–[13], and they mainly differ by the constraints imposed on the nonlinearity term. The linear-quadratic model advocated in [14] also incorporates pairwise interactions between the endmembers components. Conversely, to approximate a large range of second-order nonlinearities, Altmann *et al.* [15] introduce a polynomial post-nonlinear model that has demonstrated its ability to describe most of the nonlinear effects, in particular in vegetated areas [16]. A common feature of these models is that they all consist in including a supplementary additive term to the standard LMM, accounting for the nonlinearities. One major drawback of these models, however, is that they require to choose a specific form of nonlinearity, and this can be limiting in practice.

In this paper, a new so-called robust LMM (rLMM) is proposed. Similarly to the nonlinear models detailed above, it is built on the standard LMM and includes a supplementary additive term that accounts for nonlinear effects. However, it does not require to specify an analytical form of the nonlinearity. Instead, nonlinearities are merely treated as *outliers*. The primary motivation is that the LMM can be considered as a valid model to describe the majority of the pixels in a remotely sensed image and, as a consequence, only a *sparse* number of pixels are affected by nonlinearities. As such, one of the contributions reported in this article consists in decomposing the $L \times P$ matrix of the multi-band observations as $\mathbf{Y} \approx \mathbf{M}\mathbf{A} + \mathbf{R}$, where \mathbf{R} is a sparse (and nonnegative) residual term accounting for outliers (i.e., nonlinear effects). To reflect the assumption that the LMM holds for most of the observed pixels, the sparsity constraint is imposed at the group-level, i.e., a column of \mathbf{R} will be assumed to be either entirely zero or not. The proposed decomposition relates to *robust nonnegative matrix factorization* (rNMF) as will be explained in more details in the sequel of the paper.

The article is organized as follows. The rLMM is introduced in more details in Section II. Section III describes a block-coordinate descent algorithm for rLMM estimation. Experimental results obtained on synthetic data are reported in Section IV. Two real hyperspectral images are investigated in Section V. Section VI concludes. This article extends our preliminary conference paper [17] in a significant way. We here generalize the use of the squared Euclidean distance considered in [17] to the more general β -divergence. Additionally, we show how some of the multiplicative updates

This work is supported by the ESTOMAT PEPS Project supported by CNRS and by the Hypanema ANR Project n° ANR-12-BS03-003.

C. Févotte is with Laboratoire Lagrange (CNRS, Université de Nice Sophia Antipolis and Observatoire de la Côte d’Azur), Parc Valrose, 06108 Nice cedex 2, France. (e-mail: cedric.fevotte@unice.fr).

N. Dobigeon is with University of Toulouse, IRIT/INP-ENSEEIH, 2 rue Camichel, BP 7122, 31071 Toulouse cedex 7, France. (e-mail: nicolas.dobigeon@enseeiht.fr).

obtained heuristically in [17] can be rigorously obtained via majorization-minimization. We also describe a rule of thumb for choosing the value of the penalty weight efficiently. Finally, we provide extended experimental results on synthetical and real data.

II. ROBUST LINEAR MIXING MODEL

A. Model design

The proposed rLMM is described by

$$\mathbf{y}_p \approx \sum_{k=1}^K a_{kp} \mathbf{m}_k + \mathbf{r}_p, \quad (1)$$

where $\mathbf{y}_p = [y_{1p}, \dots, y_{Lp}]^T$ denotes the p th pixel spectrum observed in L spectral bands, $\mathbf{m}_k = [m_{1k}, \dots, m_{Lk}]^T$ denotes the k th endmember spectrum, $\mathbf{a}_p = [a_{1p}, \dots, a_{Kp}]^T$ denotes the abundances associated with the p th pixel and $\mathbf{r}_p = [r_{1p}, \dots, r_{Lp}]^T$ denotes the outlier term (accounting for nonlinearities). The matrix formulation of Eq. (1) is given by

$$\mathbf{Y} \approx \mathbf{M}\mathbf{A} + \mathbf{R}. \quad (2)$$

The approximation symbol in Eqs. (1) and (2) underlies the minimization of a measure of dissimilarity $D(\mathbf{Y}|\mathbf{M}\mathbf{A} + \mathbf{R})$, the β -divergence, that will be introduced in Section II-C.

The matrices \mathbf{Y} , \mathbf{M} and \mathbf{A} are nonnegative by nature and we take the abundance coefficients to sum to one, i.e.,

$$\mathbf{a}_p \in \mathbb{S}^K \stackrel{\text{def}}{=} \left\{ \mathbf{a} \in \mathbb{R}^K \mid a_k \geq 0, \sum_{k=1}^K a_k = 1 \right\}, \quad (3)$$

as commonly assumed in most hyperspectral data models. In this work, we assume the nonlinear component \mathbf{r}_p to be nonnegative as well, like in the bilinear models of [11]–[13] and the polynomial model with constructive interferences of [15]. As discussed in the introduction, we expect \mathbf{r}_p to be often zero, i.e., pixels to follow the standard LMM in general. For pixels where the LMM assumption fails, nonlinearities will become “active” and \mathbf{r}_p will become nonzero. This amounts to say that the energy vector

$$\mathbf{e} = [\|\mathbf{r}_1\|_2, \dots, \|\mathbf{r}_P\|_2] \quad (4)$$

is sparse. In Eq. (4), $\|\cdot\|_2$ denotes the Euclidean norm defined by $\|\mathbf{x}\|_2 = \sqrt{\sum_k x_k^2}$. Sparsity can routinely be enforced by ℓ_1 -regularization, as done next.

B. Objective function

In light of previous section, our objective is to solve the minimization problem defined by

$$\begin{aligned} \min_{\mathbf{M}, \mathbf{A}, \mathbf{R}} J(\mathbf{M}, \mathbf{A}, \mathbf{R}) &= D(\mathbf{Y}|\mathbf{M}\mathbf{A} + \mathbf{R}) + \lambda \|\mathbf{R}\|_{2,1} \\ \text{s.t. } \mathbf{M} \geq 0, \mathbf{A} \geq 0, \mathbf{R} \geq 0 &\text{ and } \|\mathbf{a}_p\|_1 = 1, \end{aligned} \quad (5)$$

where λ is a nonnegative penalty weight, $\mathbf{A} \geq 0$ denotes nonnegativity of the coefficients of \mathbf{A} , $\|\mathbf{x}\|_1 = \sum_k |x_k|$ and $\|\cdot\|_{2,1}$ is the so-called $\ell_{2,1}$ -norm defined by

$$\|\mathbf{R}\|_{2,1} = \|\mathbf{e}\|_1 = \sum_{p=1}^P \|\mathbf{r}_p\|_2. \quad (6)$$

Eq. (5) defines a robust NMF problem. Robust NMF is a nonnegative variant of robust PCA [18] which has appeared in different forms in the literature. In [19], the outlier term \mathbf{R} is nonnegative and penalized by the ℓ_1 norm. In [20] and [21], \mathbf{R} is real-valued and penalized by ℓ_1 and $\ell_{1,2}$ norms, respectively. In [22], the $\ell_{2,1}$ norm of $(\mathbf{Y} - \mathbf{M}\mathbf{A})$ is minimized (noise free scenario). A so-called robust nonnegative matrix factorization approach was introduced for the reconstruction of reflectance spectra in [23]; however the term “robust” there refers to a different feature, namely the use of a data-fitting term (the hypersurface cost function) that is less sensitive to outlier observations than the traditional squared Euclidean distance, for the computation of a regular NMF $\mathbf{Y} \approx \mathbf{M}\mathbf{A}$. Note finally that other articles that have addressed hyperspectral unmixing with regular NMF (i.e., in the standard linear model), e.g., [24]–[27].

To the best of our knowledge, the formulation of robust NMF described by Eq. (5), where \mathbf{R} is nonnegative and penalized by the $\ell_{2,1}$ norm (and where the abundances sum to one), is entirely novel. Furthermore, and most importantly, previous work [19]–[22] has only considered robust NMF with the squared Euclidean distance, i.e., $D(\mathbf{Y}|\mathbf{M}\mathbf{A} + \mathbf{R}) = \|\mathbf{Y} - \mathbf{M}\mathbf{A} - \mathbf{R}\|_2^2$ while we give here a more general formulation based on the β -divergence, defined next.

C. The β -divergence

We take the measure of fit in Eq. (5) to be such that

$$D(\mathbf{A}|\mathbf{B}) = \sum_{ij} d(a_{ij}|b_{ij}), \quad (7)$$

where $d(x|y)$ is the β -divergence between positive scalars x and y . The β -divergence was introduced in various forms in [28]–[30] and has become a standard measure of fit in NMF, see, e.g., [31]–[34]. In this paper we use the following definition:

$$d_\beta(x|y) \stackrel{\text{def}}{=} \begin{cases} \frac{x^\beta}{\beta(\beta-1)} + \frac{y^\beta}{\beta} - \frac{xy^{\beta-1}}{\beta-1} & \beta \in \mathbb{R} \setminus \{0, 1\} \\ x \log \frac{x}{y} - x + y & \beta = 1 \\ \frac{x}{y} - \log \frac{x}{y} - 1 & \beta = 0 \end{cases}. \quad (8)$$

The limiting cases $\beta = 0$ and $\beta = 1$ correspond to the Itakura-Saito and Kullback-Leibler divergences, respectively. The squared Euclidean distance is obtained for $\beta = 2$, i.e., $d_{\beta=2}(x|y) = (x - y)^2/2$. The parameter β essentially governs the assumed statistics of the observation noise and can either be fixed or learnt from training data by cross-validation. Under certain assumptions, the β -divergence can be mapped to a log-likelihood function for the Tweedie distribution [28], [35], [36], parametrized with respect to its mean. In our setting, this translates into $E[\mathbf{Y}|\mathbf{M}, \mathbf{A}, \mathbf{R}] = \mathbf{M}\mathbf{A} + \mathbf{R}$. In particular, the values $\beta = 0, 1, 2$ underlie multiplicative Gamma noise, Poisson noise and Gaussian additive noise, respectively. The β -divergence offers a continuum of noise statistics that interpolates between these three specific cases. A noteworthy property of the β -divergence is its behavior with respect to scale. Indeed, let $\lambda \in \mathbb{R}^+$, then we have $d_\beta(\lambda x|\lambda y) = \lambda^\beta d_\beta(x|y)$. This means that the data-fitting term will rely more heavily on large (resp., small) coefficients in \mathbf{Y} for $\beta > 0$ (resp., $\beta < 0$); see a more detailed discussion in [37].

III. BLOCK-COORDINATE DESCENT ALGORITHM

In order to solve the rNMF minimization problem defined at Eq. (5), we present an iterative block-coordinate descent algorithm that updates each of the parameters \mathbf{M} , \mathbf{A} and \mathbf{R} in turn. Each parameter is updated conditionally upon the current value of the other parameters and such that the objective function is decreased. This is the updating scheme employed by virtually all NMF algorithms. Unfortunately, given the non-convexity of the objective function $J(\mathbf{M}, \mathbf{A}, \mathbf{R})$, this strategy can return local solutions and proper initialization is required. This will be addressed in Section IV. The updates of the parameters are described next. In short, the parameters \mathbf{M} and \mathbf{R} are updated via majorization-minimization (MM). The parameter \mathbf{A} is updated using a heuristic scheme that has proven to work well in the literature. All the updates turn out to be “multiplicative”, i.e., such that the new update is obtained by term-to-term multiplying the previous update by a nonnegative matrix, hence automatically preserving the nonnegativity of the estimates through iterations. The resulting algorithm has linear complexity $\mathcal{O}(LKP)$ (in flops) per iteration.

A. Update of the endmember spectra \mathbf{M}

Updating \mathbf{M} given the current values of \mathbf{A} and \mathbf{R} involves solving the following minimization problem

$$\min_{\mathbf{M}} C(\mathbf{M}) = D(\mathbf{Y}|\mathbf{M}\mathbf{A} + \mathbf{R}) \text{ s.t. } \mathbf{M} \geq 0. \quad (9)$$

When $\mathbf{R} = \mathbf{0}$, this problem boils down to updating the dictionary matrix in NMF with the β -divergence. MM algorithms have been designed for that purpose in [33], [34]. In this section, we extend the MM approach to the case where $\mathbf{R} \geq \mathbf{0}$. Denote by $\tilde{\mathbf{M}}$ the estimate of \mathbf{M} at current iteration. The first step of MM consists in building an upper bound $G(\mathbf{M}|\tilde{\mathbf{M}})$ of $C(\mathbf{M})$ which is tight for $\mathbf{M} = \tilde{\mathbf{M}}$, i.e., $C(\mathbf{M}) \leq G(\mathbf{M}|\tilde{\mathbf{M}})$ for all \mathbf{M} and $C(\tilde{\mathbf{M}}) = G(\tilde{\mathbf{M}}|\tilde{\mathbf{M}})$. The second step consists in minimizing the bound with respect to (w.r.t) \mathbf{M} , producing a valid descent algorithm. Indeed, at iteration $i + 1$, it holds by construction that $C(\mathbf{M}^{(i+1)}) \leq G(\mathbf{M}^{(i+1)}|\mathbf{M}^{(i)}) \leq G(\mathbf{M}^{(i)}|\mathbf{M}^{(i)}) = C(\mathbf{M}^{(i)})$. The bound $G(\mathbf{M}|\tilde{\mathbf{M}})$ will be referred to as *auxiliary function*.

The auxiliary function obtained in [34] relies on a convex-concave decomposition of $d(x|y)$ and we follow a similar approach here. The β -divergence can always be decomposed as $d(x|y) = \tilde{d}(x|y) + \hat{d}(x|y) + \text{cst}$ where $\tilde{d}(x|y)$ and $\hat{d}(x|y)$ are respectively convex and concave functions of y and cst is constant w.r.t y . Such a decomposition is not unique; we give a “natural” decomposition in Table I. It follows that $C(\mathbf{M})$ can be decomposed as the sum of a convex term $\tilde{C}(\mathbf{M})$, a concave term $\hat{C}(\mathbf{M})$ and a constant term, such that

$$\tilde{C}(\mathbf{M}) = \sum_{lp} \tilde{d}(y_{lp}) \sum_k m_{lk} a_{kp} + r_{lp}, \quad (10)$$

$$\hat{C}(\mathbf{M}) = \sum_{lp} \hat{d}(y_{lp}) \sum_k m_{lk} a_{kp} + r_{lp}. \quad (11)$$

From there, $\tilde{C}(\mathbf{M})$ can be majorized using Jensen’s inequality, as follows. Let us denote $\tilde{y}_{lp} = \sum_k \tilde{m}_{lk} a_{kp} + r_{lp}$ the data approximation formed with the current iterate $\tilde{\mathbf{M}}$ (and recall

TABLE I
DIFFERENTIABLE CONVEX-CONCAVE DECOMPOSITION OF THE
 β -DIVERGENCE AND MM UPDATE EXPONENTS.

	$\tilde{d}(x y)$	$\hat{d}(x y)$	$\gamma(\beta)$	$\xi(\beta)$
$\beta < 1$ and $\beta \neq 0$	$-\frac{1}{\beta-1} x y^{\beta-1}$	$\frac{1}{\beta} y^\beta$	$\frac{1}{2-\beta}$	$\frac{1}{3-\beta}$
$\beta = 0$	$x y^{-1}$	$\log y$	$\frac{1}{2}$	$\frac{1}{3}$
$1 \leq \beta \leq 2$	$d(x y)$	0	1	$\frac{1}{3-\beta}$
$\beta > 2$	$\frac{1}{\beta} y^\beta$	$-\frac{1}{\beta-1} x y^{\beta-1}$	$\frac{1}{\beta-1}$	$\frac{1}{\beta-1}$

that \mathbf{A} and \mathbf{R} are here treated as constants). Then, define for $k = 1, \dots, K$, $\tilde{\lambda}_{lkp} = \tilde{m}_{lk} a_{kp} / \tilde{y}_{lp}$ and for $k = K + 1$, $\tilde{\lambda}_{lkp} = r_{lp} / \tilde{y}_{lp}$. By construction, we have $\sum_{k=1}^{K+1} \tilde{\lambda}_{lkp} = 1$. Then, using definition of convexity, we have

$$\begin{aligned} \tilde{C}(\mathbf{M}) &= \sum_{lp} \tilde{d} \left(y_{lp} \left| \sum_k \tilde{\lambda}_{lkp} \frac{m_{lk} a_{kp}}{\tilde{\lambda}_{lkp}} + \tilde{\lambda}_{l(K+1)p} \frac{r_{lp}}{\tilde{\lambda}_{l(K+1)p}} \right. \right) \\ &\leq \sum_{lp} \left[\sum_{k=1}^K \tilde{\lambda}_{lkp} \tilde{d} \left(y_{lp} \left| \frac{m_{lk} a_{kp}}{\tilde{\lambda}_{lkp}} \right. \right) \right. \\ &\quad \left. + \tilde{\lambda}_{l(K+1)p} \tilde{d} \left(y_{lp} \left| \frac{r_{lp}}{\tilde{\lambda}_{l(K+1)p}} \right. \right) \right] \\ &= \sum_{lp} \left[\sum_{k=1}^K \frac{\tilde{m}_{lk} a_{kp}}{\tilde{y}_{lp}} \tilde{d} \left(y_{lp} \left| \frac{m_{lk}}{\tilde{m}_{lk}} \right. \right) + \frac{r_{lp}}{\tilde{y}_{lp}} \tilde{d}(y_{lp} | \tilde{y}_{lp}) \right] \\ &\stackrel{\text{def}}{=} \tilde{G}(\mathbf{M}|\tilde{\mathbf{M}}) \end{aligned} \quad (12)$$

The auxiliary function essentially “breaks” the sum over k in Eq. (10) to make the optimization over \mathbf{M} separable w.r.t its entries m_{lk} .

Thanks to its concavity, $\tilde{C}(\mathbf{M})$ can be majorized by a first-order approximation at $\mathbf{M} = \tilde{\mathbf{M}}$ (the tangent inequality), leading to

$$\hat{G}(\mathbf{M}|\tilde{\mathbf{M}}) = \hat{C}(\tilde{\mathbf{M}}) + \sum_{lp} \hat{d}'(y_{lp} | \tilde{y}_{lp}) \sum_k a_{kp} (m_{lk} - \tilde{m}_{lk}), \quad (13)$$

where $\hat{d}'(x|y)$ denotes the derivative of $\hat{d}(x|y)$ w.r.t y .

An upper bound to $C(\mathbf{M})$ is finally obtained (up to constant terms) by adding $G(\mathbf{M}|\tilde{\mathbf{M}})$ and $\hat{G}(\mathbf{M}|\tilde{\mathbf{M}})$. Skipping details for brevity, the resulting function can be minimized in closed-form w.r.t \mathbf{M} , resulting in the following update

$$m_{lk} = \tilde{m}_{lk} \left(\frac{\sum_p a_{kp} y_{lp} \tilde{y}_{lp}^{\beta-2}}{\sum_p a_{kp} \tilde{y}_{lp}^{\beta-1}} \right)^{\gamma(\beta)}, \quad (14)$$

where $\gamma(\beta)$ is given in Table I and we recall that $\tilde{y}_{lp} = \sum_k \tilde{m}_{lk} a_{kp} + r_{lp}$ is the data approximation at current iteration. Note that we observed in practice that setting $\gamma(\beta) = 1$ for every value of β still reduced the objective function at every iteration and produced faster convergence. This may be interpreted as over-relaxation of the MM update, see [34] for further discussion on this subject.

B. Update of the outlier term \mathbf{R}

Updating \mathbf{R} given the current values of \mathbf{M} and \mathbf{A} involves solving the following minimization problem

$$\min_{\mathbf{R}} C(\mathbf{R}) = D(\mathbf{Y}|\mathbf{M}\mathbf{A} + \mathbf{R}) + \lambda \|\mathbf{R}\|_{2,1} \text{ s.t. } \mathbf{R} \geq 0. \quad (15)$$

The data-fitting term may be majorized using a convex-concave decomposition of $D(\mathbf{Y}|\mathbf{M}\mathbf{A} + \mathbf{R})$ exactly as we did in Section III-A. Denote by $\tilde{\mathbf{R}}$ the current update of \mathbf{R} , $s_{lp} = \sum_k m_{lk} a_{kp} = [\mathbf{M}\mathbf{A}]_{lp}$ the low-rank component and $\tilde{y}_{lp} = s_{lp} + \tilde{r}_{lp}$ the current data approximation.¹ Then, applying the Jensen and tangent inequalities to the convex and concave parts, respectively, we obtain

$$\begin{aligned} D(\mathbf{Y}|\mathbf{M}\mathbf{A} + \mathbf{R}) &\leq \sum_{lp} \left[\frac{\tilde{r}_{lp}}{\tilde{y}_{lp}} \tilde{d}(y_{lp}|\tilde{y}_{lp} \frac{r_{lp}}{\tilde{r}_{lp}}) + \frac{s_{lp}}{\tilde{y}_{lp}} \tilde{d}(y_{lp}|\tilde{y}_{lp}) \right] \\ &+ \sum_{lp} [\tilde{d}(y_{lp}|\tilde{y}_{lp}) + \tilde{d}'(y_{lp}|\tilde{y}_{lp})(r_{lp} - \tilde{r}_{lp})]. \end{aligned} \quad (16)$$

Denote by $F(\mathbf{R}|\tilde{\mathbf{R}})$ the right-hand side of Eq. (16). An auxiliary function for $C(\mathbf{R})$ may simply be obtained as $G(\mathbf{R}|\tilde{\mathbf{R}}) = F(\mathbf{R}|\tilde{\mathbf{R}}) + \lambda \|\mathbf{R}\|_{2,1}$. However, this specific auxiliary function is not amenable to optimization w.r.t \mathbf{R} (no closed-form solution). Hence, the first step of our strategy is to majorize the penalty function $\|\mathbf{R}\|_{2,1}$ as well. By concavity of the square-root function, we may write

$$\|\mathbf{R}\|_{2,1} \leq \frac{1}{2} \sum_p \left(\frac{\|\mathbf{r}_p\|_2^2}{\|\tilde{\mathbf{r}}_p\|_2} + \|\tilde{\mathbf{r}}_p\|_2 \right). \quad (17)$$

Equation (17) essentially replaces $\sqrt{\sum_l r_{lp}^2}$ by a quadratic tight upper-bound that involves $\sum_l r_{lp}^2$, with the effect of decoupling the spectral bands from within the square root. Unfortunately, the resulting auxiliary function is not yet amenable to optimization. As such, from here our approach closely follows [36]. For $\beta > 2$, we may majorize r_{lp}^2 by a monomial of degree β , matching the monomial of highest degree in $F(\mathbf{R}|\tilde{\mathbf{R}})$ (see Table I). For $\beta \leq 2$, the reverse is done: the leading monomial in $F(\mathbf{R}|\tilde{\mathbf{R}})$ is now of degree lower than 2 and may as such be majorized by a quadratic term, matching the quadratic upper bound of the penalty function; see Section 4.1 in [36] for more details. This strategy leads to the following update

$$r_{lp} = \tilde{r}_{lp} \left(\frac{y_{lp} \tilde{y}_{lp}^{\beta-2}}{\tilde{y}_{lp}^{\beta-1} + \lambda \frac{\tilde{r}_{lp}}{\|\tilde{\mathbf{r}}_p\|_2}} \right)^{\xi(\beta)}, \quad (18)$$

where $\xi(\beta)$ is the exponent given in Table I. Again, we observed in practice that setting $\xi(\beta) = 1$ for every value of β still reduced the objective function at every iteration and produced faster convergence.

¹The same notation \tilde{y}_{lp} is used for $\tilde{y}_{lp} = \sum_k \tilde{m}_{lk} a_{kp} + r_{lp}$ in Section III-A and for $\tilde{y}_{lp} = \sum_k m_{lk} a_{kp} + \tilde{r}_{lp}$ in Section III-B. Our intent is to avoid the use of too many notations and the definition of \tilde{y}_{lp} should be clear from context (i.e., which parameter update is considered).

C. Update of the abundances \mathbf{A}

Updating \mathbf{A} given the current values of \mathbf{M} and \mathbf{R} involves solving the following minimization problem

$$\min_{\mathbf{A}} C(\mathbf{A}) = D(\mathbf{Y}|\mathbf{M}\mathbf{A} + \mathbf{R}) \text{ s.t. } \mathbf{A} \geq 0 \text{ and } \forall p, \|\mathbf{a}_p\|_1 = 1. \quad (19)$$

The sum-to-one constraint on the abundances induces an extra difficulty as compared to the optimization problems involved by the updates of \mathbf{M} and \mathbf{R} . In some cases such a constraint can be handled using Lagrange multipliers, but this approach does not succeed in our setting, except in the special case $\beta = 1$, corresponding to the generalized Kullback-Leibler divergence. We hence resort to another common approach based on a change of variable. We introduce the variable \mathbf{U} to be a nonnegative matrix of dimension $K \times P$ and set

$$a_{kp} = \frac{u_{kp}}{\|\mathbf{u}_p\|_1}. \quad (20)$$

The optimization problem of Eq. (19) is turned into the new optimization problem

$$\min_{\mathbf{U}} C(\mathbf{U}) = D\left(\mathbf{Y} | \mathbf{M} \left[\frac{\mathbf{u}_1}{\|\mathbf{u}_1\|_1}, \dots, \frac{\mathbf{u}_P}{\|\mathbf{u}_P\|_1} \right] + \mathbf{R} \right) \text{ s.t. } \mathbf{U} \geq 0 \quad (21)$$

which is free from the sum-to-one constraint. This approach has been used for NMF in [38]. Unfortunately, we were not able to produce an auxiliary function for the new objective function in (21) – in particular because it can no longer be easily decomposed as a convex part and concave part. Instead, we resort to a heuristic commonly used in NMF, see, e.g., [37], [39], as follows. As it appears, the gradient of $C(\mathbf{U})$ can be expressed as the difference of two nonnegative functions such that

$$\nabla_{u_{kp}} C(\mathbf{U}) = \nabla_{u_{kp}}^+ C(\mathbf{U}) - \nabla_{u_{kp}}^- C(\mathbf{U}). \quad (22)$$

The heuristic algorithm simply writes

$$u_{kp} = \tilde{u}_{kp} \frac{\nabla_{u_{kp}}^- C(\tilde{\mathbf{U}})}{\nabla_{u_{kp}}^+ C(\tilde{\mathbf{U}})}. \quad (23)$$

It ensures nonnegativity of the parameter updates provided initialization with a nonnegative value, and produces a descent algorithm in the sense that u_{kp} is updated towards left (resp., right) when the gradient is positive (resp., negative). The algorithm was found experimentally to decrease the value of the objective function at each iteration for every of the many values of β that we tried. Denoting $\tilde{s}_{lp} = \sum_k m_{lk} \tilde{a}_{kp}$ and $\tilde{y}_{lp} = \tilde{s}_{lp} + r_{lp}$, the update is found to be

$$u_{kp} = \tilde{u}_{kp} \frac{\sum_l (m_{lk} y_{lp} \tilde{y}_{lp}^{\beta-2} + \tilde{s}_{lp} \tilde{y}_{lp}^{\beta-1})}{\sum_l (m_{lk} \tilde{y}_{lp}^{\beta-1} + \tilde{s}_{lp} y_{lp} \tilde{y}_{lp}^{\beta-2})}. \quad (24)$$

The update for \mathbf{A} is then simply $a_{kp} = u_{kp} / \|\mathbf{u}_p\|_1$.

As it turns out, the updates (14), (18) and (23) can be implemented in matrix form, as shown in Algorithm 1, which recapitulates the overall procedure. In Algorithm 1, all operators preceded by a dot ‘ \cdot ’ are entrywise MATLAB-like operations and fraction bars shall be taken term-to-term as well. Additionally, $\mathbf{1}_{M,N}$ denotes the $M \times N$ matrix with coefficients equal to 1.

Algorithm 1 Group robust NMF

```

Initialize  $\mathbf{M}$ ,  $\mathbf{A}$  and  $\mathbf{R}$ 
Set convergence tolerance parameter ‘tol’
Set value of  $\lambda$ 
 $\mathbf{S} = \mathbf{M}\mathbf{A}$ 
 $\hat{\mathbf{Y}} = \mathbf{S} + \mathbf{R}$ 
while err  $\geq$  tol do
  % Update outlier term  $\mathbf{R}$ 

   $\mathbf{R} \leftarrow \mathbf{R} \cdot \left[ \frac{\mathbf{Y} \cdot \hat{\mathbf{Y}}^{(\beta-2)}}{\hat{\mathbf{Y}}^{(\beta-1)} + \lambda \mathbf{R} \text{diag}[\|\mathbf{r}_1\|_1, \dots, \|\mathbf{r}_P\|_1]^{-1}} \right]$ 
   $\hat{\mathbf{Y}} \leftarrow \mathbf{S} + \mathbf{R}$ 

  % Update abundances  $\mathbf{A}$ 
   $\mathbf{A} \leftarrow \mathbf{A} \cdot \frac{\mathbf{M}^T (\mathbf{Y} \cdot \hat{\mathbf{Y}}^{(\beta-2)}) + \mathbf{1}_{K,L} (\mathbf{S} \cdot \hat{\mathbf{Y}}^{(\beta-1)})}{\mathbf{M}^T (\hat{\mathbf{Y}}^{(\beta-1)}) + \mathbf{1}_{K,L} (\mathbf{S} \cdot \mathbf{Y} \cdot \hat{\mathbf{Y}}^{(\beta-2)})}$ 
   $\mathbf{S} \leftarrow \mathbf{M}\mathbf{A}$ 
   $\hat{\mathbf{Y}} \leftarrow \mathbf{S} + \mathbf{R}$ 

  % Update endmembers  $\mathbf{M}$ 
   $\mathbf{M} \leftarrow \mathbf{M} \cdot \left[ \frac{(\mathbf{Y} \cdot \hat{\mathbf{Y}}^{(\beta-2)}) \mathbf{A}^T}{(\hat{\mathbf{Y}}^{(\beta-1)}) \mathbf{A}^T} \right]$ 
   $\mathbf{S} \leftarrow \mathbf{M}\mathbf{A}$ 
   $\hat{\mathbf{Y}} \leftarrow \mathbf{S} + \mathbf{R}$ 

  Compute the objective function relative decrease ‘err’ (or
  any other convergence criterion).
end while

```

D. Setting the value of λ

The hyperparameter λ controls the trade-off between the data-fitting term $D(\mathbf{Y}|\mathbf{M}\mathbf{A}+\mathbf{R})$ and the penalty term $\|\mathbf{R}\|_{2,1}$. Setting the ‘‘right’’ value of λ is a difficult task, like in any other so-called variational approach that involves a regularization term. We describe in this paragraph a rule of thumb for choosing λ in a plausible range of values. Our approach is based on the method of moments. It consists in interpreting the objective function (5) as a joint likelihood and in matching the empirical mean of the data with its prior expectation in the statistical model. As mentioned in Section II-C, the β -divergence underlies a Tweedie data distribution such that $E[\mathbf{Y}|\mathbf{M}\mathbf{A}+\mathbf{R}] = \mathbf{M}\mathbf{A} + \mathbf{R}$. The term $\lambda\|\mathbf{R}\|_{2,1}$ can be seen as a log-prior term. Using some results from [40], the corresponding prior distribution $p(r_p)$ for each column of \mathbf{R} can be obtained as a scale mixture of conditionally independent half-Normal distributions, with a Gamma distribution assigned to the scale parameter. In particular, the expectation of r_{pl} under this prior can be found to be

$$E[r_{lp}] = \frac{2}{\sqrt{\pi}} \frac{\Gamma(K/2 + 1)}{\Gamma(K/2 + 1/2)} \frac{1}{\lambda} \stackrel{\text{def}}{=} \frac{C}{\lambda}. \quad (25)$$

Let us now assume an unspecified independent prior model for $\mathbf{M}\mathbf{A}$ but such that $E[[\mathbf{M}\mathbf{A}]_{lp}] = \rho$. Denoting by $\hat{\mu} = (LP)^{-1} \sum y_{lp}$ the empirical data expectation, our approach consists in matching $\hat{\mu}$ with $E[[\mathbf{M}\mathbf{A}]_{lp}] + E[r_{lp}]$, leading to

$$\hat{\lambda} = \frac{C}{\hat{\mu} - \rho}. \quad (26)$$

We insist that the latter expression only provides a handy gross estimate of λ that comes with no statistical guarantee. In particular the estimate of λ is extremely dependent on ρ , the prior expectation of $[\mathbf{M}\mathbf{A}]_{lp}$. However, because ρ is lower bounded by 0, the estimate of λ is lower bounded by $\lambda_0 = C/\hat{\mu}$, corresponding to a plausible minimum degree of sparsity. We used $\lambda = \lambda_0$ in the evaluations below and this was found to provide satisfactory results.

IV. EXPERIMENTS WITH SYNTHETIC DATA

In this section we evaluate the relevance of the rLMM proposed in Section II and the accuracy of the corresponding rNMF algorithm described in Section III using synthetic data.

A. Data generation

Four 64×64 -pixel images composed of $K = 3$ or 6 pure spectral components have been generated according to four different linear and nonlinear models. The endmember spectra have been extracted from the spectral library provided with the ENVI software [41]. The first image, denoted as \mathcal{I}_{LMM} , is composed of pixels following the standard LMM (no nonlinear component)

$$\mathbf{y}_p = \sum_{k=1}^K a_{kp} \mathbf{m}_k + \mathbf{n}_p, \quad (27)$$

with $\mathbf{a}_p \in \mathbb{S}^K$. The three other images, denoted \mathcal{I}_{NM} , \mathcal{I}_{FM} and \mathcal{I}_{GBM} , are generated as follows. Three fourths of the image pixels are generated according to the LMM in (27) and the remaining fourth is generated according to a model that features nonlinear component interactions. More precisely, the latter pixels are generated according to:

- the Nascimento model (NM) [11]

$$\mathbf{y}_p = \sum_{k=1}^K a_{kp} \mathbf{m}_k + \sum_{i=1}^{K-1} \sum_{j=i+1}^K b_{ip} \mathbf{m}_i \odot \mathbf{m}_j + \mathbf{n}_p,$$

with

$$\begin{bmatrix} \mathbf{a}_p \\ \mathbf{b}_p \end{bmatrix} \in \mathbb{S}^{2K-1} \quad (28)$$

and $\mathbf{b}_p = [b_{1p}, \dots, b_{(K-1)p}]^T$,

- the Fan bilinear model (FM) [12]

$$\mathbf{y}_p = \sum_{k=1}^K a_{kp} \mathbf{m}_k + \sum_{i=1}^{K-1} \sum_{j=i+1}^K a_{ip} a_{jp} \mathbf{m}_i \odot \mathbf{m}_j + \mathbf{n}_p,$$

with $\mathbf{a}_p \in \mathbb{S}^K$,

- the generalized bilinear model (GBM) [15]

$$\mathbf{y}_p = \sum_{k=1}^K a_{kp} \mathbf{m}_k + \sum_{i=1}^{K-1} \sum_{j=i+1}^K \gamma_{ijp} a_{ip} a_{jp} \mathbf{m}_i \odot \mathbf{m}_j + \mathbf{n}_p,$$

with $\mathbf{a}_p \in \mathbb{S}^K$ and where the nonlinear coefficient $\gamma_{ijp} \in (0, 1)$ adjust the bilinear interaction between the i th and j th endmembers in the p th pixel.

In the models introduced above, $\mathbf{m}_i \odot \mathbf{m}_j$ stands for the termwise (Hadamard) product.

In a first experiment, the four images \mathcal{I}_{LMM} , \mathcal{I}_{NM} , \mathcal{I}_{FM} and \mathcal{I}_{GBM} have been generated by drawing the abundance coefficients \mathbf{a}_p (or $[\mathbf{a}_p^T \mathbf{b}_p^T]^T$ in the case of \mathcal{I}_{NM}) randomly and uniformly from their admissible set \mathbb{S}^K (or \mathbb{S}^{2K-1}). In a second experiment, we wanted to evaluate the robustness of the algorithms w.r.t the absence of pure pixels in the images to be unmixed. To do so, we imposed a cutoff to the abundance coefficients that removes pure pixels from the observations. As such, in this case the abundances have been uniformly drawn over a truncated version of the set defined by (3), namely

$$\mathbb{S}_{0.9}^K = \left\{ \mathbf{a} \in \mathbb{R}^K \mid a_k \geq 0, \sum_{k=1}^K a_k \leq 0.9 \right\}. \quad (29)$$

Finally, in the two experiments the interaction coefficients γ_{ijp} appearing in the GBM have been uniformly drawn over the set $(0, 1)$ and the additive noise \mathbf{n}_p was chosen white Gaussian with signal-to-noise ratio $\text{SNR} = 30\text{dB}$, which is an admissible value for most of the real imaging spectrometers.

B. Compared methods

The four images have been unmixed using rNMF and state-of-the-art algorithms specially designed for the considered models. The state-of-the-art algorithms are two-steps; the endmember matrix \mathbf{M} is estimated in a first step, and then the abundance matrix \mathbf{A} is estimated in a second step, given the endmember estimates (in a so-called “inversion” step). In contrast, rNMF performs a joint estimation of \mathbf{M} and \mathbf{A} (and \mathbf{R}).

We considered vertex component analysis (VCA) [42] coupled with fully constrained least squares (FCLS) [43]. VCA and FCLS are standard endmember extraction and inversion methods designed for the LMM. Besides, we considered the nonlinear endmember extraction technique proposed in [44], denoted as Heylen’s algorithm in what follows, coupled with four different inversion methods designed for various nonlinear models, namely the NM, FM, GBM and the very flexible polynomial post-nonlinear mixing model (PPNM) [15]. NM inversion is also achieved with FCLS since the NM can be interpreted as a linear mixture of an extended set of endmembers [11]. FM inversion is achieved with the algorithm detailed in [12], which exploits a first-order Taylor series expansion of the nonlinear term. GBM inversion is achieved with the gradient descent algorithm from [45]. Finally, PPNM inversion is addressed with the subgradient-based optimization scheme from [15].

rNMF is applied with $\beta = 2$ (reflecting the Gaussian additive noise used in the data generation and for fair comparison with the other methods that rely on this assumption as well) and $\lambda = \lambda_0$. We considered initializations by either VCA or Heylen’s algorithm. Convergence was stopped when

the relative difference between two successive values of the objective function fell under 10^{-5} .

C. Performance measures

The performance of the unmixing algorithms was evaluated in terms of endmember estimation accuracy using the average spectral angle mapper (aSAM)

$$\text{aSAM}(\mathbf{M}) = \frac{1}{K} \sum_{k=1}^K \text{acos} \left(\frac{\langle \mathbf{m}_k, \hat{\mathbf{m}}_k \rangle}{\|\mathbf{m}_k\| \|\hat{\mathbf{m}}_k\|} \right)$$

and abundance estimation accuracy using the global mean square error (GMSE)

$$\text{GMSE}^2(\mathbf{A}) = \frac{1}{KP} \sum_{p=1}^P \|\mathbf{a}_p - \hat{\mathbf{a}}_p\|^2.$$

D. Results and discussion

The performance measures returned by the unmixing methods are reported in Table II. First, the aSAM values show that the proposed rNMF algorithm competes favorably with the two considered state-of-the-art endmember extraction algorithms, namely VCA and Heylen’s algorithm. Initialized by these algorithms, it almost always improves the endmember estimation accuracy, with or without pure pixels. Similarly, when analyzing the GMSE related to abundance estimation, these results demonstrate the flexibility of the rLMM to model observations coming from various scenarios. More generally, these results demonstrate the ability of the rLMM-based unmixing technique to mitigate several kinds of nonlinear effects while preserving good estimation performance when analyzing only linear mixtures.

V. EXPERIMENTS WITH REAL DATA

In this section we apply rNMF to real hyperspectral datasets and discuss the results.

A. Description of the datasets

We consider two real hyperspectral images that have been chosen because of availability of partial ground truth. The first image was acquired over Moffett Field, CA, in 1997, by the the Airborne Visible Infrared Imaging Spectrometer (AVIRIS) [46]. Water absorption bands have been removed from the 224 spectral bands, leading to $L = 189$ spectral bands ranging from $0.4\mu\text{m}$ to $2.5\mu\text{m}$ with a nominal bandwidth of 10nm. The scene of interest, of size of 50×50 pixels, consists of a part of lake and a coastal area composed of soil and vegetation. This dataset has been previously studied in [13], [47] and, thus, the unmixing results obtained in the current work can be compared to those reported in these later references. This dataset will be referred to as the “Moffett” image in the following.

The second considered dataset was acquired by the Hypspec hyperspectral scanner over Villelongue, France, in 2010. The sensed spectral domain consists of $L = 160$ spectral bands ranging from $0.4\mu\text{m}$ to $1.0\mu\text{m}$. This image consists of a forested area where 12 vegetation species have been identified,

TABLE II

ESTIMATION PERFORMANCE IN TERM OF ASAM (\mathbf{M}) ($\times 10^{-3}$) AND GMSE² (\mathbf{A}) ($\times 10^{-3}$). BEST SCORES APPEAR IN BLUE BOLDFACE AND SECOND BEST SCORES APPEAR IN BLUE. rNMF IS INITIALIZED BY EITHER VCA OR HEYLEN’S METHOD, AS STATED BETWEEN BRACKETS. REFER TO TEXT FOR OTHER DETAILS.

			aSAM (\mathbf{M})				GMSE ² (\mathbf{A})						
			VCA	Heylen	rNMF	rNMF	VCA	Heylen				rNMF	rNMF
					(VCA)	(Heylen)		+FCLS	+NM	+FM	+GBM		
w/o pure pixels	R = 3	\mathcal{I}_{LMM}	9.71	33.86	7.65	6.78	0.10	0.06	4.32	0.07	0.07	0.07	0.04
		\mathcal{I}_{NM}	12.74	170.50	202.05	256.71	20.78	73.79	78.34	96.23	91.85	54.68	82.80
		\mathcal{I}_{FM}	7.12	102.26	7.55	29.61	0.84	13.54	38.17	13.28	14.83	0.71	1.57
		\mathcal{I}_{GBM}	8.26	33.10	5.69	5.02	0.25	0.23	4.01	0.07	0.08	0.20	0.20
	R = 6	\mathcal{I}_{LMM}	72.33	86.10	23.03	24.92	2.74	2.90	26.03	2.84	2.76	0.27	0.77
		\mathcal{I}_{NM}	175.97	249.60	156.81	238.68	53.40	49.00	75.31	74.87	70.38	32.12	32.46
		\mathcal{I}_{FM}	93.28	187.55	144.74	259.01	13.67	34.71	68.13	39.01	34.51	10.41	19.86
		\mathcal{I}_{GBM}	79.24	106.52	83.08	85.49	4.55	5.73	32.21	5.50	4.31	4.95	4.57
with pure pixels	R = 3	\mathcal{I}_{LMM}	46.45	64.89	12.37	11.91	1.89	2.05	11.85	2.07	2.06	0.16	0.14
		\mathcal{I}_{NM}	46.40	176.29	189.76	254.58	23.94	66.17	67.18	91.05	92.78	52.77	68.75
		\mathcal{I}_{FM}	52.77	214.15	9.26	239.32	4.03	107.59	104.75	96.43	115.65	0.79	20.07
		\mathcal{I}_{GBM}	48.18	58.58	9.49	9.31	2.66	2.48	5.85	1.77	1.58	0.30	0.29
	R = 6	\mathcal{I}_{LMM}	66.55	79.19	15.72	17.67	3.95	2.34	24.35	2.07	2.11	0.63	0.39
		\mathcal{I}_{NM}	224.81	112.82	101.07	265.25	63.85	16.88	68.20	39.56	41.66	30.93	28.94
		\mathcal{I}_{FM}	98.16	171.10	145.41	198.64	11.21	28.55	56.15	30.30	28.64	9.28	10.20
		\mathcal{I}_{GBM}	75.21	136.20	79.34	156.75	5.36	16.75	40.60	16.72	16.68	5.06	10.93

during the Madonna project [48]. The sub-image of interest, of size of 50×50 pixels, is known to be mainly composed of oak and chestnut trees, with an additional unknown non-planted-tree endmember (referred to as Endm. #3 in what follows). This dataset will be referred to as the “Madonna” image in the following.

B. Selection of β via induction

Most of the literature in hyperspectral unmixing uses the squared Euclidean distance for the data-fitting term. This choice is often driven by common practice rather than physical motivations stemming from the nature of the data. As mentioned in paragraph II-C, divergences are often log-likelihoods in disguise, and as such, choosing a divergence is akin to making a noise assumption. Thus, when no obvious physical model supports the choice of a specific divergence, finding the “right” measure of fit can be seen as a model selection problem. When data with a ground truth is available for a specific task, a model can be selected based on its performance for this task. Unfortunately, and to the best of our knowledge, no such public real hyperspectral data exists for spectral unmixing, i.e., with perfectly known endmember spectra and corresponding abundance coefficients. Another way of selecting a model can be based on its ability to predict unseen or missing data. Such an approach does not require a ground truth. As such, in this paragraph we study how NMF with the β -divergence performs on an interpolation task. Pixels are randomly removed from real hyperspectral images and those pixels are reconstructed from the low-rank approximation. The process is repeated for various values of β and an optimal value of β (in terms of predicting performance) is deduced.

More precisely, 25, 50 or 75% of the pixels have been randomly and uniformly removed from the ‘Moffett’ and

“Madonna” images described in paragraph V-A. Then, we fitted a low rank approximation \mathbf{MA} to the remaining pixels by minimizing

$$\sum_{(l,p) \in \mathcal{O}} d_{\beta}(y_{lp} | [\mathbf{MA}]_{lp}) \quad (30)$$

with respect to \mathbf{M} and \mathbf{A} , where \mathcal{O} denotes the set of observed entries. The outlier term \mathbf{R} is omitted in this experiment as it cannot be inferred for the missing entries (there is one outlier entry per missing data entry and the problem is not identifiable). The objective function (30) can be minimized using a minor modification of the MM algorithm described in Section III, similarly to the factorizations with missing data described in [34], [49].

After estimation, the missing pixels (l,p) belonging to the complement of \mathcal{O} are reconstructed as $[\mathbf{MA}]_{lp}$ and the aSAMs values between the original (complete) data \mathbf{Y} and its reconstruction $\hat{\mathbf{Y}}$ are computed. This process is repeated for values of β from -1 to 3 with a step-size of 0.5 . For every value of β , 10 runs are considered, corresponding to different random initializations and different sets of missing pixels. The number of endmembers was set to $K = 3$.

The results of the experiment are displayed in Figure 1. They show that: (1) the choice of β matters, (2) best performance is achieved for $\beta = 1$ for the Moffett image and $\beta = 1.5$ for the Madonna image, with values of β in the $[0, 2]$ range yielding sensibly similar performance. The conclusion of this study is that it can be worth using alternatives to the standard squared Euclidean distance for hyperspectral unmixing (such as the KL divergence, corresponding to $\beta = 1$), if it does not come with extra difficulties in the optimization (as such, the MM algorithm is equally simple to implement for all values of β).

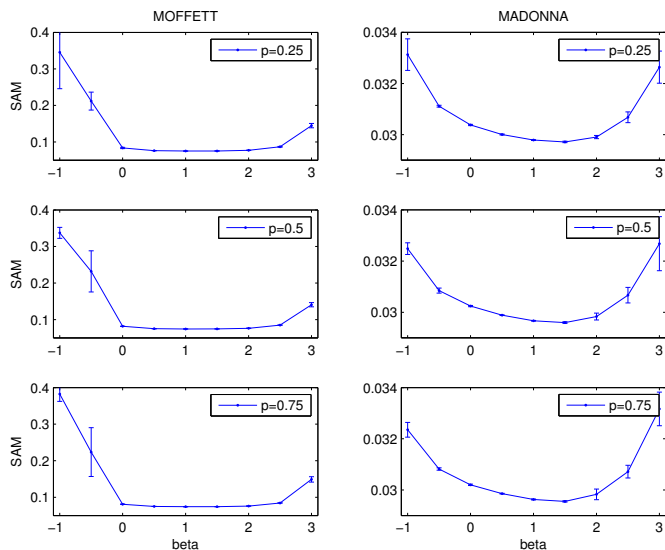


Fig. 1. Average SAM values (\pm standard deviation) between the original and reconstructed data over 10 runs. The percentage of observed entries is increased from 25% (top) to 75% (bottom). Left: Moffett image; Right: Madonna image. Best reconstructions are obtained for either $\beta = 1$ or 1.5.

C. Robust unmixing results

In a last experiment, the proposed rLMM-unmixing technique has been applied on the real Moffett and Madonna images. We used $K = 3$ and considered two values of β , namely $\beta = 1$ (Kullback-Leibler divergence) and $\beta = 2$ (squared Euclidean distance). The endmember spectra and abundance maps estimated by rNMF are depicted in Fig. 2. For conciseness, only the abundance maps obtained with $\beta = 1$ are displayed as the results for $\beta = 2$ were visually very similar.

The unmixing results are in good agreement with previous results [47], [50]. However, in addition to the standard description of the data by linearly mixed endmembers, the proposed model also provides information regarding the pixels that cannot be explained with the standard LMM. As such, Fig. 3 displays the energy $e = [\|r_1\|_2, \dots, \|r_P\|_2]$ of the residual component estimated by rNMF. Regarding the Moffett image, the maps demonstrate that most of the pixels of this scene can be accurately described using the LMM. However, some few pixels, mainly located in the lake shore, appear at outliers. These pixels probably correspond to areas where some interactions between several endmembers occur (e.g., water/vegetation, water/soil). Similar results have been already observed in [13], [51], which confirms the relevance of the proposed method. For the Madonna image, the energy map exhibits residual terms that are mainly located in the area occupied by the oak trees and the unknown 3rd endmember. Furthermore, the image shows regular vertical patterns that are almost surely due to a sensor defect or miscalibration during the data post-processing.

VI. CONCLUSION

In this paper we have presented a new mixing model to describe hyperspectral data. This model, denoted as rLMM, extends the standard LMM by including a residual term that

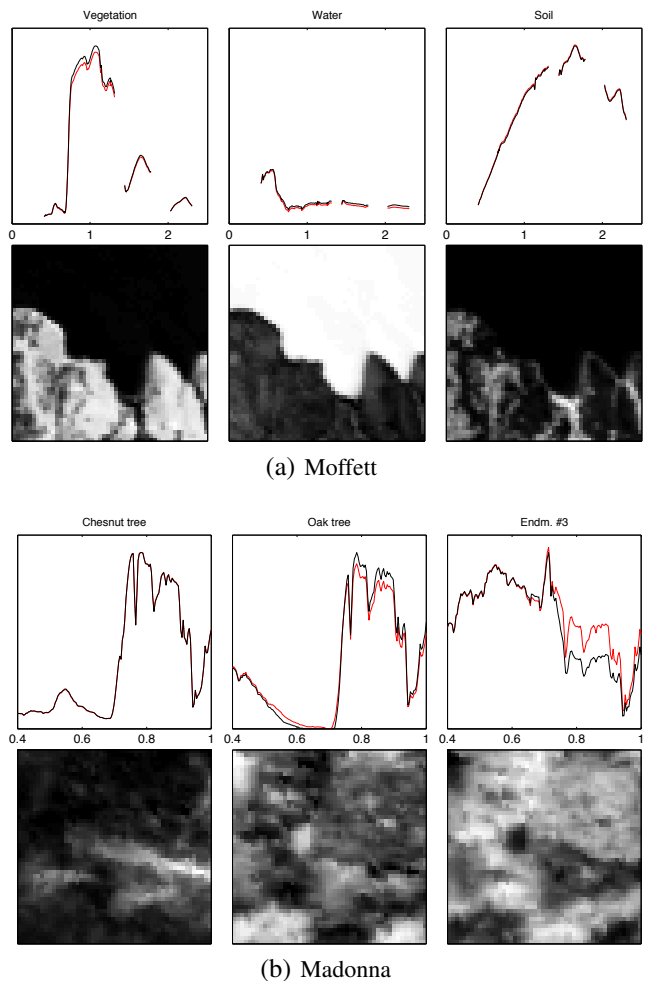


Fig. 2. Unmixing results of two real hyperspectral images. Top of each image: endmembers estimated by the proposed rNMF-based unmixing algorithm with $\beta = 1$ (red lines) and $\beta = 2$ (black lines). Bottom of each image: estimated abundance maps obtained for $\beta = 1$; black (resp. white) pixels correspond to absence (resp. presence) of the associated endmembers.

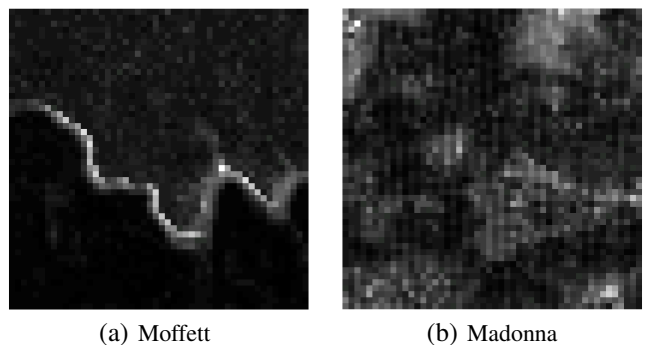


Fig. 3. Energy of the nonlinear components returned by rNMF with $\beta = 1$. Dark (resp. light) pixels correspond to small (resp. large) values.

can capture so-called nonlinear effects. These nonlinear effects are treated as additive and sparsely active outliers. In contrast with state-of-the-art literature on nonlinear hyperspectral unmixing, our approach does not require the specification of a particular model of nonlinearity.

The resulting unmixing problem was formulated as a new form of robust NMF problem, for which we developed a

simple and effective block-coordinate descent algorithm that involves multiplicative updates. We provided an effective rule of thumb for setting the value of the penalty weight, which leaves our algorithm virtually free of parameters (only the number of endmembers needs to be specified). Simulations conducted on synthetic and real data have illustrated the relevance of rLMM, which outperformed many unmixing methods designed for various linear and nonlinear models.

ACKNOWLEDGEMENTS

We thank Vincent Y. F. Tan and Zhao Renbo from National University of Singapore for discussions related to robust NMF and feedback about this manuscript.

REFERENCES

- [1] G. P. Asner and K. B. Heidebrecht, "Spectral unmixing of vegetation, soil and dry carbon cover in arid regions: comparing multispectral and hyperspectral observations," *Int. J. Remote Sens.*, vol. 23, no. 19, pp. 3939–3958, Oct. 2002.
- [2] K. E. Themelis, F. Schmidt, O. Sykioti, A. A. Rontogiannis, K. D. Koutroumbas, and I. A. Daglis, "On the unmixing of MEX/OMEGA hyperspectral data," *Planetary and Space Science*, vol. 68, no. 1, pp. 34–41, 2012.
- [3] A. Gowen, C. O'Donnell, P. Cullen, G. Downey, and J. Frias, "Hyperspectral imaging : an emerging process analytical tool for food quality and safety control," *Trends in Food Science & Technology*, vol. 18, no. 12, pp. 590–598, 2007.
- [4] N. Dobigeon and N. Brun, "Spectral mixture analysis of EELS spectrum-images," *Ultramicroscopy*, vol. 120, pp. 25–34, Sept. 2012.
- [5] N. Keshava and J. F. Mustard, "Spectral unmixing," *IEEE Signal Process. Mag.*, vol. 19, no. 1, pp. 44–57, Jan. 2002.
- [6] J. M. Bioucas-Dias, A. Plaza, N. Dobigeon, M. Parente, Q. Du, P. Gader, and J. Chanussot, "Hyperspectral unmixing overview: Geometrical, statistical, and sparse regression-based approaches," *IEEE J. Sel. Topics Appl. Earth Observations and Remote Sens.*, vol. 5, no. 2, pp. 354–379, April 2012.
- [7] N. Dobigeon, J.-Y. Tourneret, C. Richard, J. C. M. Bermudez, S. McLaughlin, and A. O. Hero, "Nonlinear unmixing of hyperspectral images: Models and algorithms," *IEEE Signal Process. Mag.*, vol. 31, no. 1, pp. 89–94, Jan. 2014.
- [8] B. Somers, K. Cools, S. Delalieux, J. Stuckens, D. V. der Zande, W. W. Verstraeten, and P. Coppin, "Nonlinear hyperspectral mixture analysis for tree cover estimates in orchards," *Remote Sens. Environment*, vol. 113, pp. 1183–1193, Feb. 2009.
- [9] B. Somers, L. Tits, and P. Coppin, "Quantifying nonlinear spectral mixing in vegetated areas: computer simulation model validation and first results," *IEEE J. Sel. Topics Appl. Earth Observations and Remote Sens.*, 2014, to appear.
- [10] Y. Altmann, N. Dobigeon, and J.-Y. Tourneret, "Bilinear models for nonlinear unmixing of hyperspectral images," in *Proc. IEEE GRSS Workshop Hyperspectral Image Signal Process.: Evolution in Remote Sens. (WHISPERS)*, Lisbon, Portugal, June 2011, pp. 1–4.
- [11] J. M. P. Nascimento and J. M. Bioucas-Dias, "Nonlinear mixture model for hyperspectral unmixing," in *Proc. SPIE Image and Signal Processing for Remote Sensing XV*, L. Bruzzone, C. Notarnicola, and F. Posa, Eds., vol. 7477, no. 1. SPIE, 2009, p. 747701.
- [12] W. Fan, B. Hu, J. Miller, and M. Li, "Comparative study between a new nonlinear model and common linear model for analysing laboratory simulated-forest hyperspectral data," *Int. J. Remote Sens.*, vol. 30, no. 11, pp. 2951–2962, June 2009.
- [13] A. Halimi, Y. Altmann, N. Dobigeon, and J.-Y. Tourneret, "Nonlinear unmixing of hyperspectral images using a generalized bilinear model," *IEEE Trans. Geosci. and Remote Sensing*, vol. 49, no. 11, pp. 4153–4162, Nov. 2011.
- [14] I. Meganem, P. Déliot, X. Briottet, Y. Deville, and S. Hosseini, "Linear-quadratic mixing model for reflectances in urban environments," *IEEE Trans. Geosci. and Remote Sensing*, vol. 52, no. 1, pp. 544–558, Jan. 2014.
- [15] Y. Altmann, A. Halimi, N. Dobigeon, and J.-Y. Tourneret, "Supervised nonlinear spectral unmixing using a post-nonlinear mixing model for hyperspectral imagery," *IEEE Trans. Image Process.*, vol. 21, no. 6, pp. 3017–3025, June 2012.
- [16] N. Dobigeon, L. Tits, B. Somers, Y. Altmann, and P. Coppin, "A comparison of nonlinear mixing models for vegetated areas using simulated and real hyperspectral data," *IEEE J. Sel. Topics Appl. Earth Observations and Remote Sens.*, submitted. [Online]. Available: <http://arxiv.org/abs/1312.1270/>
- [17] N. Dobigeon and C. Févotte, "Robust nonnegative matrix factorization for nonlinear unmixing of hyperspectral images," in *Proc. IEEE Workshop Hyperspectral image and signal processing: Evolution in remote sensing (WHISPERS)*, Gainesville, FL, 2013.
- [18] E. J. Candès, X. Li, Y. Ma, and J. Wright, "Robust principal component analysis?" *Journal of ACM*, vol. 58, no. 1, pp. 1–37, 2009.
- [19] P. Sprechmann, A. Bronstein, and G. Sapiro, "Real-time online singing voice separation from monaural recordings using robust low-rank modeling," in *Proc. Int. Soc. Music Information Retrieval Conf. (ISMIR)*, Porto, Portugal, Oct. 2012.
- [20] L. Zhang, Z. Chen, M. Zheng, and X. He, "Robust nonnegative matrix factorization," *Front. Electr. Electron. Eng. China*, vol. 6, no. 2, pp. 192–200, 2011.
- [21] B. Shen, L. Si, R. Ji, and B. Liu, "Robust nonnegative matrix factorization via ℓ_1 norm regularization," *ArXiv preprint*, 2012. [Online]. Available: <http://arxiv.org/abs/1204.2311/>
- [22] D. Kong, C. Ding, and H. Huang, "Robust nonnegative matrix factorization using ℓ_{21} -norm," in *Proc. 20th ACM Int. Conf. Information and Knowledge Management*, 2011, pp. 673–682.
- [23] A. Ben Hamza and D. J. Brady, "Reconstruction of reflectance spectra using robust nonnegative matrix factorizations," *IEEE Trans. Signal Process.*, vol. 54, pp. 3637–3642, 2006.
- [24] V. P. Pauca, J. Piper, and R. J. Plemmons, "Nonnegative matrix factorization for spectral data analysis," *Linear Algebra and its Applications*, vol. 416, pp. 29–47, 2006.
- [25] L. Miao and H. Qi, "Endmember extraction from highly mixed data using minimum volume constrained nonnegative matrix factorization," *IEEE Trans. Geosci. and Remote Sensing*, vol. 45, no. 3, pp. 765–777, 2007.
- [26] Z. Yang, G. Zhou, S. Xie, S. Ding, J.-M. Yang, and J. Zhang, "Blind spectral unmixing based on sparse nonnegative matrix factorization," *IEEE Trans. Image Process.*, vol. 20, no. 4, pp. 1112–1125, 2011.
- [27] E. Esser, M. Moller, S. Osher, G. Sapiro, and J. Xin, "A convex model for nonnegative matrix factorization and dimensionality reduction on physical space," *IEEE Trans. Image Process.*, vol. 21, no. 7, pp. 3239–3252, 2012.
- [28] B. Jørgensen, "Exponential dispersion models," *J. Roy. Stat. Soc. Ser. B*, vol. 49, no. 2, pp. 127–162, 1987.
- [29] A. Basu, I. R. Harris, N. L. Hjort, and M. C. Jones, "Robust and efficient estimation by minimising a density power divergence," *Biometrika*, vol. 85, no. 3, pp. 549–559, Sept. 1998.
- [30] A. Cichocki and S. Amari, "Families of Alpha- Beta- and Gamma-divergences: Flexible and robust measures of similarities," *Entropy*, vol. 12, no. 6, pp. 1532–1568, June 2010.
- [31] R. Kompass, "A generalized divergence measure for nonnegative matrix factorization," *Neural Computation*, vol. 19, no. 3, pp. 780–791, 2007.
- [32] A. Cichocki, R. Zdunek, and S. Amari, "Csiszar's divergences for non-negative matrix factorization: Family of new algorithms," in *Proc. 6th International Conference on Independent Component Analysis and Blind Signal Separation (ICA)*, Charleston SC, USA, Mar. 2006, pp. 32–39.
- [33] M. Nakano, H. Kameoka, J. Le Roux, Y. Kitano, N. Ono, and S. Sagayama, "Convergence-guaranteed multiplicative algorithms for non-negative matrix factorization with beta-divergence," in *Proc. IEEE Workshop Mach. Learning for Signal Process. (MLSP)*, Sept. 2010.
- [34] C. Févotte and J. Idier, "Algorithms for nonnegative matrix factorization with the beta-divergence," *Neural Computation*, vol. 23, no. 9, pp. 2421–2456, Sept. 2011.
- [35] M. Tweedie, "An index which distinguishes between some important exponential families," in *Proc. Indian Stat. Inst. Golden Jubilee Int. Conf.*, ser. Statistics: Applications and New Directions, J. K. Ghosh and J. Roy, Eds., Calcutta, India, 1984, pp. 579–604.
- [36] V. Y. F. Tan and C. Févotte, "Automatic relevance determination in nonnegative matrix factorization with the beta-divergence," *IEEE Trans. Patt. Anal. Mach. Intell.*, vol. 35, no. 7, pp. 1592 – 1605, July 2013.
- [37] C. Févotte, N. Bertin, and J.-L. Durrieu, "Nonnegative matrix factorization with the Itakura-Saito divergence. With application to music analysis," *Neural Computation*, vol. 21, no. 3, pp. 793–830, Mar. 2009.
- [38] J. Eggert and E. Körner, "Sparse coding and NMF," in *Proc. IEEE International Joint Conference on Neural Networks*, 2004, pp. 2529–2533.

- [39] T. Virtanen, "Monaural sound source separation by non-negative matrix factorization with temporal continuity and sparseness criteria," *IEEE Trans. Audio, Speech, Language Process.*, vol. 15, no. 3, pp. 1066–1074, Mar. 2007.
- [40] A. Lee, F. Caron, A. Doucet, and C. Holmes, "A Hierarchical Bayesian Framework for Constructing Sparsity-inducing Priors," *arXiv.org*, Sept. 2010.
- [41] RSI (Research Systems Inc.), *ENVI User's guide Version 4.0*, Boulder, CO 80301 USA, Sept. 2003.
- [42] J. M. Nascimento and J. M. Bioucas-Dias, "Vertex component analysis: a fast algorithm to unmix hyperspectral data," *IEEE Trans. Geosci. and Remote Sensing*, vol. 43, no. 4, pp. 898–910, April 2005.
- [43] D. C. Heinz and C. -I Chang, "Fully constrained least-squares linear spectral mixture analysis method for material quantification in hyperspectral imagery," *IEEE Trans. Geosci. and Remote Sensing*, vol. 29, no. 3, pp. 529–545, March 2001.
- [44] R. Heylen, D. Burazerovic, and P. Scheunders, "Non-linear spectral unmixing by geodesic simplex volume maximization," *IEEE J. Sel. Topics Signal Process.*, vol. 5, no. 3, pp. 534–542, June 2011.
- [45] A. Halimi, Y. Altmann, N. Dobigeon, and J.-Y. Tourneret, "Unmixing hyperspectral images using the generalized bilinear model," in *Proc. IEEE Int. Conf. Geosci. Remote Sens. (IGARSS)*, Vancouver, Canada, July 2011, pp. 1886–1889.
- [46] Jet Propulsion Lab. (JPL), "Avisar free data," California Inst. Technol., Pasadena, CA, 2006. [Online]. Available: <http://aviris.jpl.nasa.gov/html/aviris.freedata.html>
- [47] N. Dobigeon, J.-Y. Tourneret, and C.-I Chang, "Semi-supervised linear spectral unmixing using a hierarchical Bayesian model for hyperspectral imagery," *IEEE Trans. Signal Process.*, vol. 56, no. 7, pp. 2684–2695, July 2008.
- [48] D. Sheeren, M. Fauvel, S. Ladet, A. Jacquin, G. Bertoni, and A. Gibon, "Mapping ash tree colonization in an agricultural mountain landscape: Investigating the potential of hyperspectral imagery," in *Proc. IEEE Int. Conf. Geosci. Remote Sens. (IGARSS)*, Vancouver, Canada, July 2011, pp. 3672–3675.
- [49] N.-D. Ho, "Nonnegative matrix factorization algorithms and applications," Ph.D. dissertation, Universit Catholique de Louvain, 2008. [Online]. Available: www.inma.ucl.ac.be/~vdooren/ThesisHo.pdf
- [50] Y. Altmann, N. Dobigeon, S. McLaughlin, and J.-Y. Tourneret, "Non-linear spectral unmixing of hyperspectral images using Gaussian processes," *IEEE Trans. Signal Process.*, vol. 61, no. 10, pp. 2442–2453, May 2013.
- [51] O. Besson, N. Dobigeon, and J.-Y. Tourneret, "Minimum mean square distance estimation of a subspace," *IEEE Trans. Signal Process.*, vol. 59, no. 12, pp. 5709–5720, Dec. 2011.

Nicolas Dobigeon received the state engineering degree in electrical engineering from ENSEEIHT, Toulouse, France, and the M.Sc. degree in signal processing from the National Polytechnic Institute of Toulouse (INP Toulouse), both in June 2004, as well as the Ph.D. degree and Habilitation à Diriger des Recherches in Signal Processing from the INP Toulouse in 2007 and 2012, respectively. He was a Post-Doctoral Research Associate with the Department of Electrical Engineering and Computer Science, University of Michigan, Ann Arbor, MI, USA, from 2007 to 2008. Since 2008, he has been with the National Polytechnic Institute of Toulouse (INP-ENSEEIHT, University of Toulouse) where he is currently an Associate Professor. He conducts his research within the Signal and Communications Group of the IRIT Laboratory and he is also an affiliated faculty member of the Telecommunications for Space and Aeronautics (TeSA) cooperative laboratory. His current research interests include statistical signal and image processing, with a particular interest in Bayesian inverse problems with applications to remote sensing, biomedical imaging and genomics.

Cédric Févotte received the state engineering and PhD degrees in control and computer science from the École Centrale de Nantes, France, in 2000 and 2003, respectively. During his PhD, he was with the Signal Processing Group at the Institut de Recherche en Communication et Cybernétique de Nantes (IRCCyN). From 2003 to 2006, he was a research associate with the Signal Processing Laboratory at the University of Cambridge (Engineering Department). He was then a research engineer with the music editing technology start-up company Mist-Technologies (now Audionamix) in Paris. In 2007, he became a CNRS tenured researcher. He was affiliated with LTCI (CNRS & Télécom ParisTech) from 2007 to 2012. Since 2013, he has been with Laboratoire Lagrange (CNRS, Observatoire de la Côte d'Azur & Université de Nice Sophia Antipolis). His research interests generally concern statistical signal processing and machine learning, in particular for inverse problems and source separation. He is a member of the IEEE "Machine Learning for Signal Processing" technical committee.